ELSEVIER

3D optomechanical metamaterials

Alexander Münchinger [1,*], Li-Yun Hsu [2,3], Franziska Fürniß [1], Eva Blasco [2,3,4],
Martin Wegener [1,4,*]

[1] Institute of Applied Physics, Karlsruhe Institute of Technology (KIT), 76128 Karlsruhe, Germany
[2] Centre for Advanced Materials (CAM), Ruprecht-Karls-Universität Heidelberg, Im Neuenheimer Feld 225, 69120 Heidelberg, Germany
[3] Institute of Organic Chemistry, Ruprecht-Karls-Universität Heidelberg, Im Neuenheimer Feld 270, 69120 Heidelberg, Germany
[4] Institute of Nanotechnology, Karlsruhe Institute of Technology (KIT), 76128 Karlsruhe, Germany

Ideally, many materials should have a "knob" that allows for changing its properties at will, including the possibility to flip the sign of its behavior. This "knob" could be used to continuously tune the properties or in the sense of a digital switch. Such extreme level of stimulus–responsiveness has come into reach with recently increased possibilities of manufacturing complex rationally designed artificial materials called metamaterials on the micrometer scale. Here, we present mechanical metamaterials composed of liquid–crystal elastomers, whose director field is arranged into a designed complex three-dimensional (3D) pattern during the 3D laser printing process. External light from a blue LED, with intensities in the range of 10–30 W/cm^2, serves as the stimulus. In the first example, we repeatedly flip the sign of the Poisson's ratio of an achiral architecture within classical elasticity. In the second example, we flip the sign of the twist per strain in a chiral metamaterial beyond classical elasticity. The presented examples overcome major limitations in responsive mechanical metamaterials and we foresee many possible three-dimensional responsive micro-architectures manufactured along these lines.

Keywords: 3D two-photon lithography; 4D printing; Liquid crystal elastomer; Responsive 3D metamaterials

Introduction

Metamaterials mainly derive their effective properties from their designed microstructure, rather than from the constituent material they are made of (for recent progress see [1–4]). Therefore, if one is able to change the microstructure significantly by applying an external stimulus [5,6], one is able to change the effective metamaterial properties. For example, a metamaterial could change its mechanical properties upon irradiation with sun light to automatically adjust the lighting conditions, change its appearance, or to control room temperature. Stimulus–responsive metamaterials could serve as adjustable stretch benches for biological cells [7]. As another example, elastic wave propagation and polarization could be controlled locally by light, perhaps even in the sense of space–time metamaterials [8,9]. Previous experiments along these lines have been performed [10–31] using temperature [10–16], pressure [17], solvents [18], electrical voltage [19,20], static magnetic fields [21–29] or light [30,31] as stimulus. However, these experiments were restricted to macroscopic models [10,11,13,15–17,20–30], to effectively-two-dimensional architectures [11,13–16,18,19,21–25,27,28,30,31], or had a limited material-parameter tuning range [12], especially not including the extreme possibility to flip the sign of a material parameter by light.

* Corresponding authors.
E-mail addresses: Münchinger, A. (alexander.muenchinger@kit.edu), Wegener, M. (martin.wegener@kit.edu).

Please cite this article in press as: A. Münchinger et al., Materials Today (2022), https://doi.org/10.1016/j.mattod.2022.08.020

Here, we go significantly beyond this previous work and consider mechanical metamaterials within and beyond classical elasticity that can be stimulated by light, opening the field of 3D optomechanical metamaterials. We start from a liquid–crystal elastomer [32–35] and construct beams with two different director orientations. It is well known and crucial for our work that oriented liquid–crystal elastomers behave anisotropically due to the anisotropy of the polymer network which is induced by the mesogenic nature of the monomers [32]. Therefore, an equal stimulus imposed onto the two liquid–crystal–elastomer parts of a beam leads to a pronounced bending of this bi-material element. Next, we construct a metamaterial mechanism based on a number of these bending elements. The first case lies within classical elasticity and is based on bow-tie elements in a tetragonal metamaterial crystal. The bow-tie is a paradigmatic motif in auxetic metamaterials [36], and has been studied in great detail [37–42]. The shape change of the bow-tie elements leads to a transition from non-auxetic to auxetic behavior, *i.e.*, the Poisson's ratio flips sign from positive to negative. The second case

goes beyond classical elasticity into the realm of chiral micropolar elasticity and is based on chiral elements on the surfaces of connected cubes within a tetragonal metamaterial unit cell. The stimulus-induced change of the handedness of the chiral elements leads to a flip in sign of the twist per strain. For both cases, we directly measure the effective metamaterial behavior by applying a displacement along one crystallographic direction and by quantifying the behavior on a sub-unit-cell scale by optical-microscopy digital image analysis.

Results

A key technological requirement for this route is the ability to manufacture three-dimensional (3D) liquid–crystal–elastomer microstructures for which the local liquid–crystal director at any point inside of the structure can be oriented along any targeted direction. This crucial technology has recently become available [43]. It is based on combining two-photon 3D laser printing with the ability to apply a quasi-static electric field with
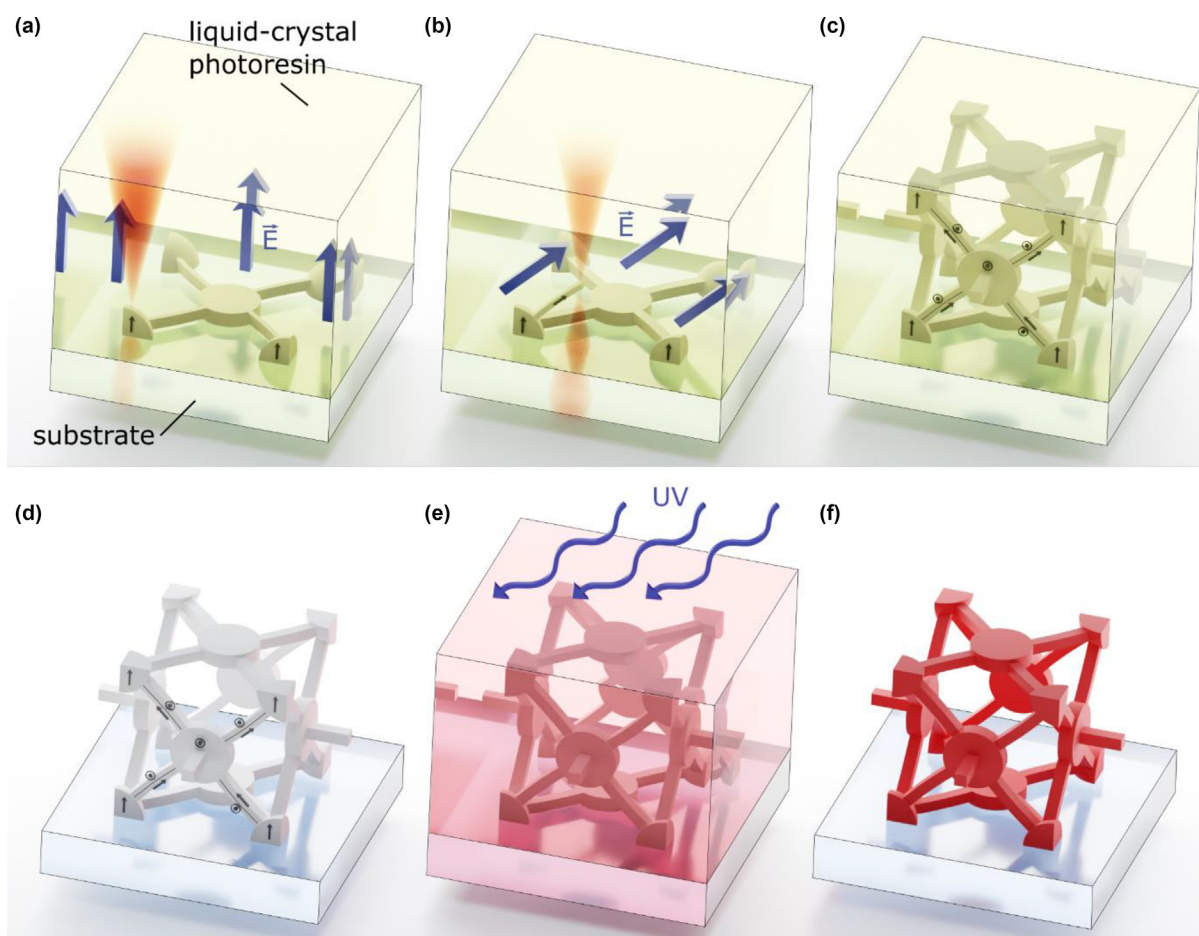
FIGURE 1

Defining the three-dimensional liquid–crystal-director field. (a) The liquid–crystal director of the photoresin is aligned *via* an applied quasi-static electric field, $\vec{E}$, and locally fixed by two-photon polymerization (printing) of a voxel. (b) Next, the electric-field orientation can be changed for printing another part of the structure with a different director orientation. Importantly, the previously printed polymer parts do not change their director orientation. (c) In the stage after completing the printing, the structure contains polymerized and unpolymerized regions. (d) The insufficiently polymerized parts are washed out in the development process, leaving behind a polymerized structure comprising a targeted three-dimensional liquid–crystal-director field. At this stage, the sample is optically transparent. (e) Next, the sample is immersed in a solution containing Disperse Red 1 Methacrylate, which diffuses into the structure. This dye serves as an absorber to couple to the stimulus light. The dye molecules are covalently attached acrylate groups of not fully reacted monomers within the printed structure by means of UV irradiation. (f) After washing, the final metamaterial structure appears red.

SHORT COMMUNICATION

RESEARCH: Short Communication

variable orientation in-situ during the printing process within the printing zone, as illustrated in Fig. 1a–d (see Methods).

To introduce absorber molecules to the metamaterial structure that couple to the external light serving as stimulus, the structures are immersed in a solution containing Disperse Red 1 Methacrylate (Fig. 1e), which diffuses into the printed structure. After washing (Fig. 1f), the dye is attached to the printed structure resulting in the photoresponsive three-dimensional metamaterial microstructures that we employ for experiments. The molar extinction coefficient of the dye is plotted in Fig. S3.

Here, we use a new and refined liquid–crystal photoresin, which is illustrated in Fig. 2a. With respect to our previous work [43], we reduce the content of E7, which otherwise tends to evaporate from the printed structures at elevated temperatures, thereby leading to sample deterioration. Owing to this step, we arrive at a largely improved long-time behavior under cyclic ramping of the sample temperature. This aspect is evidenced by the exemplary data shown in Fig. 2b. In our below photo-thermal experiments, the local sample temperature is proportional to the local heating power due to absorption of light. Therefore, in practice, the lifetime of our metamaterial samples is only limited by bleaching of the light-absorbing molecules after extended periods of light illumination. The mechanism underlying this bleaching has been discussed in [44]. As a result, after extensive illumination with light, one can see the bleaching by comparing the optical images of the samples before and after usage (as exemplified for the auxetic metamaterial in Fig. S8). In principle, new dye molecules can be infiltrated to "refresh" the sample. Further details of this manufacturing approach and our new photoresin are given in the Methods section. In Fig. S7, we show that the repeatability upon temperature cycling of the photoresin used here has largely improved with respect to that of our previous work.

Figs. 3 and 4 summarize our results on two different elastic-metamaterial designs and their response with respect to illumination by light. For the experiments on both, we use a light-emitting diode (LED). Its emission spectrum peaks around 450 nm wavelength (see Fig. S3). We estimate an average light intensity of 23.6W/cm^2 at an electrical current of $I = 1\text{A}$ through the LED. In what follows, we quote the LED current I as the main parameter because this is the quantity over which we have direct control in our experiments. In the theoretical modelling, we compute the resulting temperature field within the metamaterial. To model the resulting thermal expansion, we incorporate a fit to the measured thermal strain depicted in Fig. 2b. Thereby, we obtain the structural changes of the metamaterials and their resulting effective properties.

The first metamaterial we discuss is built from the bow-tie element depicted in Fig. 3a. It comprises a spatial distribution of two orthogonal horizontal director orientations, which are illustrated by the red and orange color code. A metamaterial sample consisting of $3 \times 3 \times 5$ of such bow-tie unit cells is depicted in the electron micrograph in Fig. 3b and in the light-microscope image in Fig. 3c. The red color in this image is due to the infiltrated dye, which absorbs the light of the LED used as the external stimulus.

The measured Poisson's ratio of this sample versus LED current, derived from the behavior of the three central layers (see Methods), is represented by the small black dots in Fig. 3d. The large black dots are the average over four individual measurements for each LED current. The averaged Poisson's ratio decreases monotonically from a positive Poisson's ratio of 0.47 for zero LED current to a negative ratio of -0.27 for an LED current of $I = 1.5\text{A}$.

Bright-field light-microscope images for both cases are depicted in Fig. 3e for two different LED currents. For the large LED current of $I = 1.5\text{A}$, one can clearly see the strong lateral contraction of the bow-tie elements in the central layers of the sample that leads to the negative Poisson's ratio. The bow-tie elements in layer 4, counted from the base plate, contract less than in layers 2 and 3 because of an attenuation of the LED light passing the metamaterial due to absorption and the directional characteristics of the LED. There is little contraction at the top and
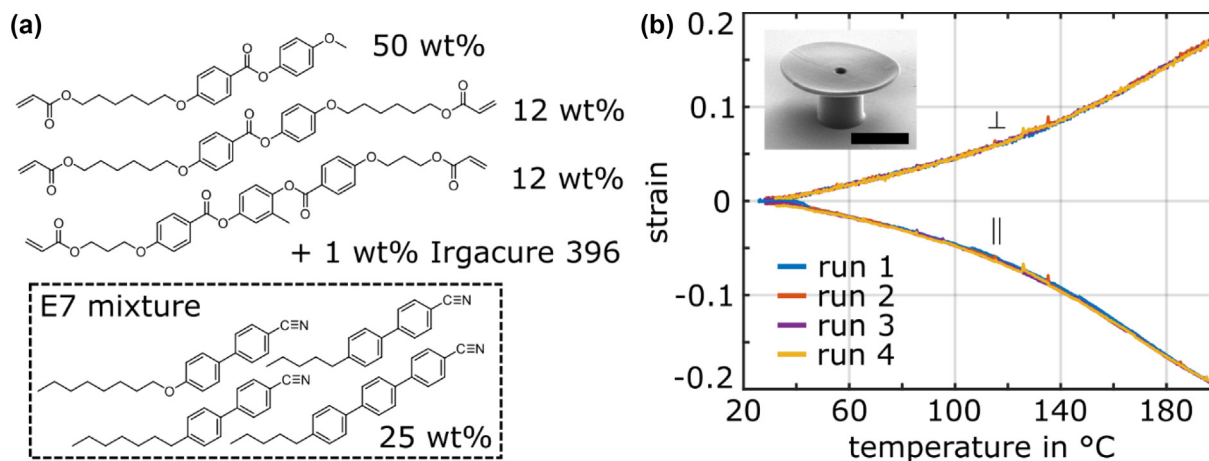
FIGURE 2

Photoresin composition and behavior. (a) Chemical structure and composition of the used photoresin. (b) The measured strain of a printed liquid–crystal–elastomer disk on a cylindrical post (see inset, scale bar 30 μm) is plotted versus the applied temperature. For increasing temperature, the material contracts parallel to the director axis (∥) and expands perpendicular (⊥) to it. The measurement has been repeated four times (see legend) with strains as large as about ±0.2. The overlap of the four curves within the linewidth indicates reversible and repeatable stimulus-responsive behavior. Further evidence for the repeatability under conditions of large deformations is given in Fig. 3d and f.
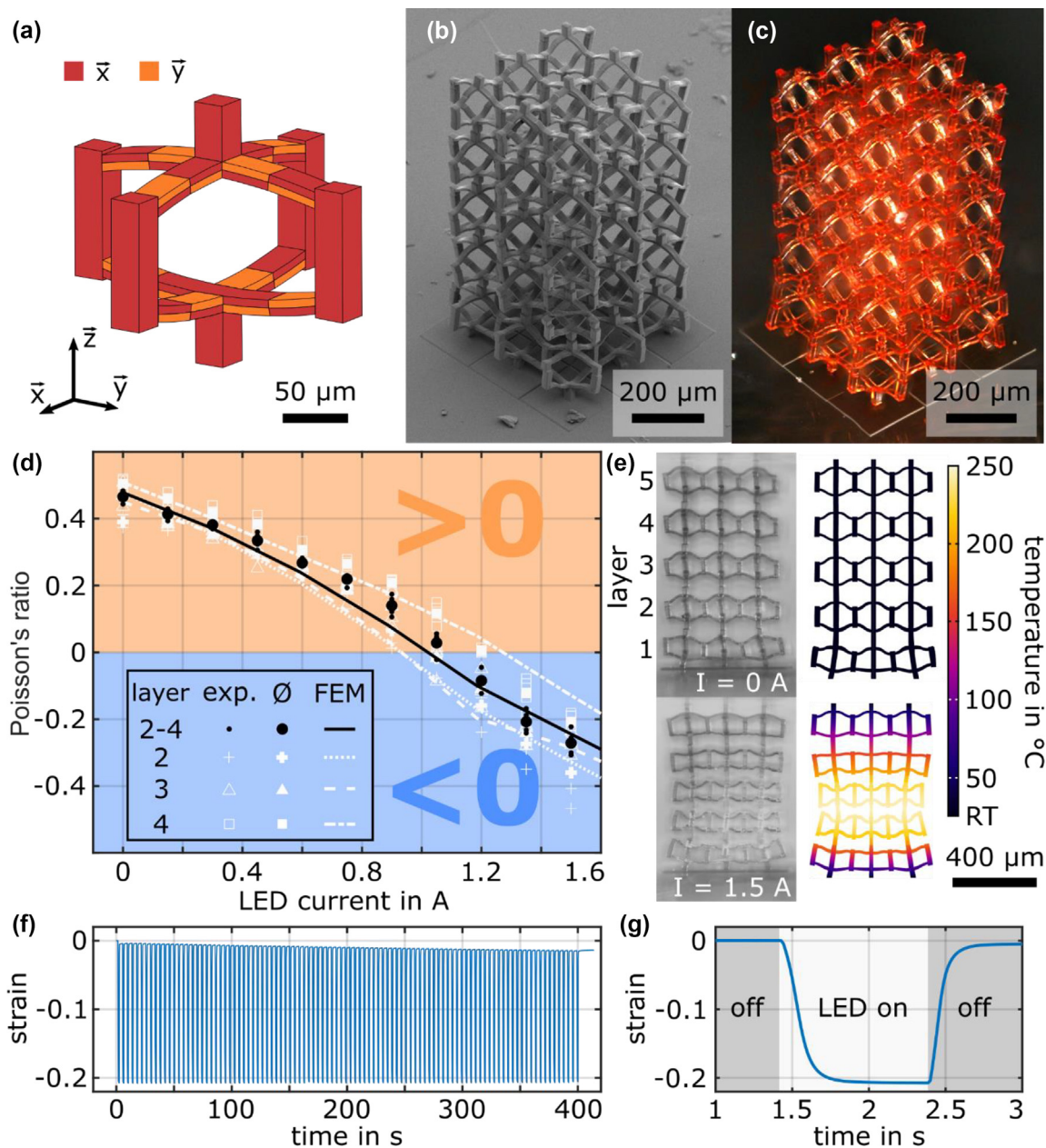
3

FIGURE 3

Light-tunable auxetic metamaterial. (a) Illustration of the print file of one bow-tie element. The design contains two different local director orientations (see legend). (b) Electron micrograph of a printed metamaterial sample. (c) Light microscope image of the same sample. The red color is due to the infiltrated absorber dye. (d) The individual measurements of the Poisson's ratio with respect to layers 2–4 (small black dots) is shown versus the LED current. The average over four independent measurements is indicated by large black dots. The Poisson's ratios obtained from numerical finite-element calculations are represented by the solid black line. The corresponding data for the individual layers are indicated by the white curves (see legend). (e) Light-microscope images of the unstrained sample for two different LED currents ($I = 0\text{A}$, $I = 1.5\text{A}$) compared to cuts through geometries retrieved from numerical finite-element calculations. The calculated temperature profile is illustrated by a false-color plot. The corresponding strain field is given in Fig. S4. (f) Measured strain versus time for 100 switching cycles. In each cycle, the LED is turned on at $I = 1.0\text{A}$ for a time span of 1s and turned off for 3s. (g) Zoom into the first cycle.

bottom layers of the metamaterial since it is connected to the glass substrates there. Due to the high thermal conductivity of the substrates, the local temperature stays close to the ambient temperature at these points. Therefore, the resulting thermal strain is close to zero.

Due to these different contraction levels of the different layers, we also plot the Poisson's ratio for the individual layers in Fig. 3d. These data are represented by the white symbols (see

legend). As expected from our above discussion, at a given LED current, the Poisson's ratio is larger in layer 4 than in layers 2 and 3.

To further test our understanding of the metamaterial behavior, we have performed extensive finite-element calculations. Due to the large strains, these calculations must account for geometrical nonlinearities (see Methods). These multi-physics calculations also account for the aforementioned inhomogeneous
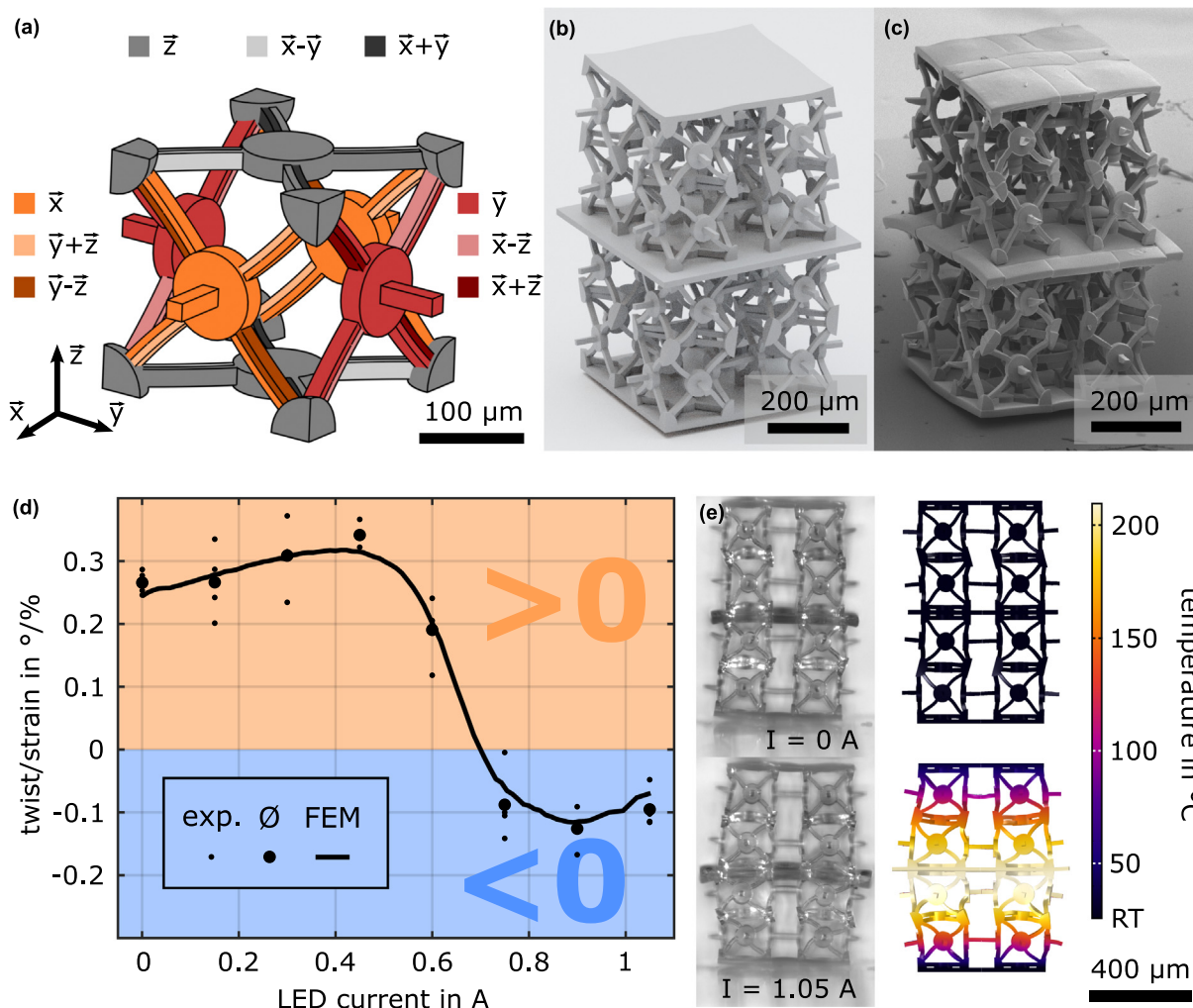
4

FIGURE 4

Light-tunable chiral elastic metamaterial. (a) Blueprint of the print file for the chiral metamaterial unit cell, including nine different orientations of the local liquid–crystal director (see color code in legend). (b) Calculated sample structure after development, especially including the effects of anisotropic shrinkage. The blueprint shown in panel (a) anticipates this deformation. (c) Electron micrograph of a printed metamaterial sample, which is in excellent agreement with panel (b). (d) Four independent sets of measurements of twist per strain (small black dots) versus the electrical current I sent through the LED. In each set, the current has been ramped up from zero to the maximum value. During these measurements, the LED has been switched on for about 15 minutes and the qualitative behaviour is reproducible. The large black dots represent the average over four independent measurements. The solid curve results from numerical finite-element calculations. (e) Light-microscope images of the unstrained sample at two different LED currents ($I = 0$A, $I = 1.05$A). Both images are compared side-by-side to cuts through the three-dimensional geometries resulting from finite-element calculations. The calculated temperature profile is added onto the geometries by false colors.

temperature distribution within the metamaterial specimen. The calculated behavior depicted by the different curves in Fig. 3d (see legend) is in good agreement with the experimental data shown in the same panel. Furthermore, selected examples of two-dimensional cuts through the calculated metamaterial structure are depicted in Fig. 3e ($I = 0$ and $I = 1.5$A). For both cases, the metamaterial structure is in good agreement with the light microscope images depicted in the same panel. This indicates that the printed microstructure and liquid–crystal-director arrangement are sufficiently close to the target (Fig. 3a) and that we understand the mechanisms underlying the observed deformations.

To study the reversibility and repeatability of the metamaterial behavior, we have turned on the LED for 1s with $I = 1$A and turned it off for 3s for 100 cycles. The overall strain of the sample versus time is depicted in Fig. 3f. For all cycles, the sample reaches a maximum strain of about 21%. However, the sample does not completely recover to its initial height within one cycle. The initial strain decreases by about 0.4% within the first cycle and by 0.01% every following cycle. This behavior might be due to viscoelasticity and/or plastic deformations. Indeed, our finite-element calculations show local strains of up to 60% within the metamaterial during actuation. However, even after 100 cycles, these effects are small compared to the overall actuation of the metamaterial. A movie of the first two cycles is depicted in Supplementary Video 1.

Fig. 3g shows a zoom into the data of Fig. 3f for the first actuation cycle. From fitting exponentials to the data, we deduce a photo-thermal time constant of 75 ± 1ms for the actuation and

63 ± 2ms for the recovery. Conceptually, the two time constants need not be identical. The actuation time is connected to how fast the system is heated locally, which depends on the light intensity applied, whereas the recovery time is connected to cooling *via* heat conduction.

To test whether the observed actuation is actually due to the absorption of light by the dye molecules (cf. Fig. 1e), we have performed control experiments without this dye. For an LED current of $I = 1$A, we obtain a 400 times reduced strain with respect to the samples that contain the absorber dye. This evidently shows that the dye is the main converter of the incident light into heat. A movie of an undyed sample illuminated by the LED is provided by Supplementary Video 2.

The second metamaterial we examine is made from the chiral unit cell depicted in Fig. 4a. It includes nine different orientations of the director, namely the three orthogonal Cartesian axis and the six face diagonals. Such unit cells are known to respond with a twist if a strain is applied along an axis [45]. Here, we chose the z–axis.

Fig. 4c shows an electron micrograph of a metamaterial sample. It consists of $2 \times 2 \times 2$ unit cells followed by the same amount of inverted unit cells, with a central plate in between. Due to this configuration (see [45]), the twists cancel at the top and the bottom of the sample, eliminating the need for sliding boundary conditions. The twist of the central plate, divided by the axial strain is the material parameter we monitor versus the LED light level. Fig. 4d shows the results of four independent individual experiments (small black dots) and their average (large black dots). The solid curve is the result of a numerical finite-element calculation (see Methods), which agrees well with the experimental data. Specifically, at around an LED current of 0.7A, the twist/strain flips sign. This sign flip originates from a change in handedness of the metamaterial unit cells, as can directly be seen from the images in Fig. 4e. This can also be observed in Supplementary Video 3 showing the actuation of the sample. It is known that the magnitude of the twist/strain depends on the shape of the unit cell and on the number of unit cells in the metamaterial specimen (see Fig. S5 for zero LED current and [45,46]).

Conclusion and discussion

In conclusion, we have described a classical (Cauchy) linear-elastic metamaterial and a non-classical micropolar chiral meta-material for which the sign of an effective material parameter can be flipped by illuminating the specimen by blue light from an LED at light intensities around $10 - 30$W/cm^2. Our approach takes advantage of the recently emerged capability to 3D print on the micrometer scale complex three-dimensional distributions of the liquid–crystal-director field. By our proof-of-principle experiments, we have overcome previous limitations in the field of responsive mechanical metamaterials, which are either macroscopic models, two dimensional or show only a limited parameter tuning range. For example, the chiral architectures could be applied in the sense of optically controlling the sign of acoustical activity [47]. With further improvements in regard to sample quality and number of unit cells contained, many further possibilities for stimulus–responsive designed material architectures

arise. For example, optomechanical metamaterials responsive to sun light as mentioned in the introduction would become possible.

Materials and methods

Printing setup

The used two-photon printer was already described elsewhere [43]. Herein, the applied electric field, $\vec{E}$, orients the liquid–crystal director within a liquid photoresin (Fig. 1a). Two-photon absorption of focused light from a femtosecond laser locally polymerizes the photoresin and fixes the local liquid–crystal-director orientation within the tight laser focus. When printing the next volume element ("voxel"), the direction of the electric-field vector can be changed, including as possibilities the orthogonal Cartesian axes as well as all face and body diagonals (Fig. 1b). In this manner, nearly arbitrary director fields can be realized within the photoresin (Fig. 1c). After development, this pattern translates into an optically transparent sample (Fig. 1d). Compared to the setup described in [43], we replaced the femtosecond laser by a Chameleon Ultra II from Coherent.

Photoresin preparation

To prepare the photoresin, 4-Methoxybenzoic acid 4-(6-acryloyloxyhexyloxy)phenyl ester (50 wt%), 4-(6-(Acryloyloxy) hexyloxy)phenyl 4-(6-(acryloyloxy)hexyloxy)benzoate (12 wt %), 1,4-Bis-[4-(3-acryloyloxypropyloxy)benzoyloxy]-2-methyl benzene (12 wt%), E7 mixture (25 wt%) and Irgacure 369 (1 wt %) were added to a vial and heated to 80 °C under constant stirring until all the components were dissolved. Afterwards, the resin was filtered with a 0.45 μm PTFE syringe filter with a diameter of 13 mm to remove insoluble remains. Before printing, the resin was heated to 80 °C to ensure a homogeneous solution. All mesogens were bought from SYNTHON Chemicals GmbH & Co. KG and used as delivered.

Adding 4-(6-(Acryloyloxy)hexyloxy)phenyl 4-(6-(acryloyloxy) hexyloxy)benzoate to the resist was inspired by the experiments performed by McCracken et al. They found that the crystalline to nematic transition temperature of their resist dropped drastically by adding this component. [48] This might explain the increased solubility of the acrylates in E7, which allowed the reduction of E7 in the resist composition.

Printing parameters

For the manufacturing of the metamaterial structures, we used a hatching distance of 0.2 μm and a slicing distance of 0.5 μm. The scan speed was 50 mm s^{-1} while the laser power was about 116 mW for a vertical director orientation, 104 mW for a diagonal director orientation and 78 mW for a horizontal director orientation. The laser powers were measured at the entrance pupil of the objective lens. The pulse duration at the entrance pupil was measured to be 166 fs, while the pulse repetition rate was 80 MHz. The center wavelength of the laser was 790 nm. The employed electric fields were on average 0.4 V μm^{-1} for horizontal director orientations, on average 0.5 V μm^{-1} for diagonal director orientations and on average 0.7 V μm^{-1} for a vertical director orientation.

Sample development

We developed all samples in ethanol at room temperature for 15 minutes. Afterwards, we dried the sample in a critical-point dryer to prevent damage during the evaporation of ethanol. This procedure resulted in a shrinkage of about 14% perpendicular to the director and negligible shrinkage along the director.

Dyeing procedure

To dye the metamaterial samples, we dissolved 1 mg Disperse Red 1 Methacrylate and 0.1 mg Irgacure 819 in 0.1 ml of a 10: 1 mixture of isopropanol and dichloromethane. The developed sample was clamped in a PTFE holder and covered with about 0.05 ml of the dye solution. To prevent evaporation, we covered the holder with a coverslip. To incorporate the dye covalently into the printed polymer network, we illuminated the sample by a UV LED for about 1 hour. The employed LED (VL-4.LC @ 254 nm) was placed at a distance of about 2 cm. After illumination, we washed the sample in ethanol and dried it in a critical-point dryer.

Strain versus temperature

To measure the strain versus temperature behavior of the resulting liquid–crystal elastomer, we printed thin disks with a designed radius of 35 μm and a thickness of 1.5 μm supported by a cylindrical beam with a diameter of 12.5 μm and a height of 30 μm. The director was parallel to the disk. After development, the disk was elliptical with a major axis of about 70 μm and a minor axis of about 60 μm, which results in a shrinkage of about 14% perpendicular to the director. The sample was placed in an Instec mk2000 heating stage mounted in a light microscope. While recording a video, we heated the sample to 200 °C with a rate of 10 °C min^{-1}. We refocused the disk every minute to keep the image sharp. In the resulting video we fitted ellipses to the boundary of the disk in every frame and estimated the diameter of the ellipse along and perpendicular to the director. Thereby, we were able to calculate the strain versus temperature behavior plotted in Fig. 2b.

LED characterization

To estimate the power of the light irradiated by the LED (Osram LE B P1W FY-W), we brought it in contact to a power sensor (Thorlabs S170C) and measured the power for an LED current low enough to not saturate the sensor. Next, we increased the distance between LED and sensor and measured the power versus LED current up to 1.5 A. With the first measurement of the LED in close contact with the sensor, we were able to calculate the full power irradiated by the LED for currents up to 1.5 A. Assuming a Lambertian emitter, we estimated the intensity at the base of a sample glued to the LED. The resulting intensity is plotted in Fig. S2.

Metamaterial properties characterization

To bring a metamaterial sample as close as possible to the active region of the LED, we directly glued (Marabu Fixogum) the substrate of the sample onto the window covering the LED. Thereby, the sample was at a distance of about 0.9 mm from the active region of the LED. The LED itself is mounted on a motorized linear stage. The sample was opposed by a glass sheet, on which the sample was pushed to apply a strain. The glass sheet was covered with immersion oil (Zeiss Immersol 518F) to prevent the sample to stick to the glass sheet. During the experiment, the sample was observed via two microscopes from the side and from the top through the glass sheet. The setup is illustrated in Fig. S1.

For every data point in Fig. 3d and Fig. 4d, we performed the following steps. First, we turned on the LED with the specified current I while the sample was not in contact with the glass sheet. This led to a shape shift of the metamaterial induced by the LED illumination. In the presence of this new shape and while the LED illumination is kept on, we manually drove the top of the sample to the glass sheet. We took care to not yet apply a strain on the sample. At this position, we took an optical image from the side. For the second metamaterial, we additionally took an image of the central plate from the top. These images represent the unstrained reference configuration for the current I. This was followed by the application of a strain to the sample via the motorized linear stage. We applied about 3% axial strain to the first metamaterial sample and about 1.8% strain to the second metamaterial sample. In this configuration we also took an image from the side and an image from the top. These images represent the strained configuration of the sample for the LED current I. From these images, the Poisson's ratio and the twist per strain are derived (see below). Afterwards we released the strain via the stage and turned off the LED.

To track changes between the microscope images of the unstrained and the strained configuration, we employed image cross correlation. We selected prominent features in the microscope image of the unstrained configuration and searched for the same feature in the microscope image of the strained configuration. Thereby, we determined the displacement of that feature with subpixel precision [49].

To evaluate the Poisson's ratio for the first metamaterial example, we tracked the position of the top and the bottom of every unit cell and the top left, top right, bottom left and bottom right corner of every layer. From that we calculated the average height and width of every layer in the unstrained and strained configuration. With that we calculated the vertical and horizontal strain of the strained configuration with respect to the unstrained configuration. Dividing the negative horizontal strain by the vertical strain resulted in the Poisson's ratio plotted in white in Fig. 3d. For the data plotted in black, we calculated the average width and height of the central three layers instead and calculated the Poisson's ratio from that as described for a single layer. This procedure is graphically illustrated in Fig. S6. In the Supplementary, we also provide the formulas we have used to extract the effective metamaterial Poisson's ratio as a function of the LED illumination current.

For the second metamaterial example, we tracked the top and the bottom of the sample in the side view and the edges of the central plate in the top view. The overall twist per strain of the sample was calculated by dividing the rotation angle of the central plate by the strain of the whole sample, which is plotted in Fig. 4d.

Repeatability and reversibility characterization

We fixed the sample as described above on the LED. The LED was biased with $I = 1.0$ A for one second and turned off for 3 seconds

for 100 cycles *via* a computer-controlled power supply. With a microscope looking from the side, we recorded a video with 70 frames per second. Using image cross-correlation analysis, we determined the vertical extent of the sample in every frame of the video and calculated the strain of the sample, which is depicted in Fig. 3f and Fig. 3g.

Finite-element calculations

For the finite-element calculations, we employed the structural mechanics module of COMSOL Multiphysics. Due to the large expected deformations, we accounted for geometrical non-linearities. For simplicity we assumed a linear elastic model for the constituent material with a homogeneous and isotropic Young's modulus of $E = 20$ MPa and a Poisson's ratio of $v = 0.45$. To calculate the response of the structure to an anisotropic strain field, we employed the thermal expansion module which allows to apply a strain at every point of the structure. To simulate the expected shape after shrinkage, for example, we applied a strain of -14.2% perpendicular to the director at every point of the structure.

To calculate the response of a sample to the LED, we first calculated a corresponding temperature profile within the sample *via* a simplified model. This temperature was then translated *via* the data displayed in Fig. 2b into a strain. The resulting strain was applied to the sample at every point as described above. To obtain the simplified temperature profile, we assumed the sample to stay at room temperature T_R at the top and bottom where it has contact to glass substrates. This agrees with the observation that the samples only weakly react to the LED at those positions. Furthermore, we assumed a spatial heat source $Q(z) = Q_0 e^{-\alpha z}$ resulting from absorption of the light. It decays exponentially from the bottom to the top of the sample. The exponential decay accounts for the decay of the light intensity due to absorption following Beer's law and the directional characteristics of the LED. For a homogeneous sample with height h, these assumptions result in the following temperature profile:

$$T(z) = \frac{T_p - T_R}{f} \times \left(e^{-\alpha z} - 1 - \left(e^{-\alpha h} - 1 \right) \times \frac{z}{h} \right) + T_R$$

$$f = e^{-\alpha z_p} - 1 - \left(e^{-\alpha h} - 1 \right) \times \frac{z_p}{h}$$

$$z_p = -\frac{1}{\alpha} \ln \left(\frac{1 - e^{-\alpha h}}{\alpha h} \right)$$

For our metamaterial structures, we obtained a good agreement with the experiments by assuming $\alpha = 2/845 \mu m^{-1}$. There, α also accounts for the geometry of the sample. The parameter T_p is the peak temperature of the distribution. In the experiment it is proportional to the LED current. The proportionality factor depends on the geometry of the sample and the concentration of the dye. It is therefore different for the two different metamaterial samples. We obtained good agreement with our experiments by choosing $T_p = 135 \frac{K}{A} \times I + T_R$ for the first metamaterial and $T_p = 175 \frac{K}{A} \times I + T_R$ for the second metamaterial.

To numerically calculate the Poisson's ratio of the first metamaterial sample, we performed two steps similar to the experiment. First, we calculated the deformed geometry for a certain LED current only with the bottom of the sample fixed. There, we probed for the height of the resulting deformed geometry. In a second step, we used this information to apply a displacement to the top of the sample to obtain a strain of 3% as in the experiment. In both configurations, we probed for the height and width of every layer similar to the experiment and performed the same evaluation as for the experimental data. The results are plotted as solid lines in Fig. 3d.

We performed similar simulations to obtain the twist per strain for the second metamaterial. In the first step, we applied a displacement of 20 μm perpendicular to the outer boundary of the base plate to simulate the partial detachment of the base-plate observed in the electron micrograph of the printed sample. With this boundary condition, we again calculated the deformed geometry for a certain LED current. We probed for the height of the sample and applied an axial strain of 1.8% to the sample in a second simulation with the same LED current and the same boundary condition for the base plate. We probed for the rotation of the central plate and calculated the twist per strain plotted in Fig. 4d from that quantity.

Funding

Data Availlabilty Statement

The data that support the findings of this study are openly available in the KITopen repository at https://doi.org/10.5445/IR/1000150677.

CRediT authorship contribution statement

Alexander Münchinger: Writing – review & editing, Visualization, Project administration, Writing – original draft, Software, Methodology, Formal analysis, Investigation, Conceptualization, Data curation, Validation. **Li-Yun Hsu:** Writing – review & editing, Methodology, Resources. **Franziska Fürniß:** Software. **Eva Blasco:** Writing – review & editing, Supervision, Resources. **Martin Wegener:** Supervision, Funding acquisition, Writing – review & editing, Writing – original draft, Resources, Conceptualization.

Declaration of Competing Interest

The authors declare that they have no known competing financial interests or personal relationships that could have appeared to influence the work reported in this paper.

Appendix A. Supplementary data

Supplementary data (The Supplementary Videos were recorded with an optical light microscope. The depicted samples are

mounted on an LED as described in the methods. The LED current was 1 A for all videos) to this article can be found online at https://doi.org/10.1016/j.mattod.2022.08.020.

References

[1] K. Bertoldi et al., Nat. Rev. Mater. 2 (2017) 1–11.
[2] M. Kadic et al., Nat. Rev. Phys. 1 (2019) 198–210.
[3] J.U. Surjadi et al., Adv. Eng. Mater. 21 (2019) 1800864.
[4] J. Fan et al., Mater. Today 50 (2021) 303–328.
[5] S.M. Montgomery et al., Curr. Opin. Solid State Mater. Sci. 24 (2020) 100869.
[6] J. Qi et al., Adv. Sci. 9 (2022) 2102662.
[7] M. Hippler et al., Sci. Adv. 6 (2020) eabc2648.
[8] G.W. Milton, O. Mattei, Proc. Math. Phys. Eng. Sci. 473 (2017) 20160819.
[9] S. Xu, C. Wu, Phys. Rev. Lett. 120 (2018) 096401.
[10] C. Yang et al., Mater. Horiz. 6 (2019) 1244–1250.
[11] D. Wang et al., Mater. Interfaces 12 (2020) 22146–22156.
[12] Q. Ji et al., Commun. Mater. 2 (2021) 1–6.
[13] L.M. Korpas et al., Mater. Interfaces 13 (2021) 31163–31170.
[14] W. Zhang et al., Nat. Commun. 12 (2021) 112.
[15] J. Mueller, J.A. Lewis, K. Bertoldi, Adv. Funct. Mater. 32 (2022) 2105128.
[16] Z. Wang et al., Sci. Adv. 6 (2020) eabc0034.
[17] Y. Wang et al., Nature 596 (2021) 238–243.
[18] C. Delaney et al., J. Mater. Chem. C 9 (2021) 11674–11678.
[19] Y.H. Fu et al., Adv. Funct. Mater. 21 (2011) 3589–3594.
[20] C. Luo et al., Mater. Horiz. 7 (2020) 229–235.
[21] M. Lapine et al., Nat. Mater. 11 (2012) 30–33.
[22] J.N. Grima et al., Smart Mater. Struct. 22 (2013) 084016.
[23] Z. Wang et al., Adv. Mater. 28 (2016) 9857–9861.
[24] O.R. Bilal, A. Foehr, C. Daraio, Adv. Mater. 29 (2017) 1700628.
[25] Y. Kim et al., Nature 558 (2018) 274–279.
[26] K. Yu et al., Adv. Mater. 30 (2018) 1706348.
[27] S.M. Montgomery et al., Adv. Funct. Mater. 31 (2021) 2005319.
[28] Y. Alapan et al., Sci. Adv. 6 (2020) eabc6414.
[29] J.A. Jackson et al., Sci. Adv. 4 (2018) eaau6419.
[30] A.S. Gliozzi et al., Nat. Commun. 11 (2020) 1–8.
[31] S. Nocentini et al., Adv. Opt. Mater. 6 (2018) 1800167.
[32] T.J. White, D.J. Broer, Nat. Mater. 14 (2015) 1087–1098.
[33] M.O. Saed, A. Gablier, E.M. Terentjev, Chem. Rev. 122 (2022) 4927–4945.
[34] M. del Pozo et al., Adv. Mater. 34 (2022) 2104390.
[35] C.A. Spiegel et al., Adv. Funct. Mater. 30 (2020) 1907615.
[36] X. Ren et al., Smart Mater. Struct. 27 (2018) 023001.
[37] L.J. Gibson et al., Proc. R. Soc. A: Math. Phys. Sci. 382 (1982) 25–42.
[38] I.G. Masters, K.E. Evans, Compos. Struct. 35 (1996) 403–422.
[39] C.W. Smith, J.N. Grima, K.E. Evans, Acta Mater. 48 (2000) 4349–4356.
[40] J. Schwerdtfeger et al., Phys. Status Solidi B 247 (2010) 269–272.
[41] T. Bückmann et al., Adv. Mater. 24 (2012) 2710–2714.
[42] L. Yang et al., Int. J. Solids Struct. 69–70 (2015) 475–490.
[43] A. Münchinger et al., Adv. Mater. Technol. 7 (2022) 2100944.
[44] T.L. Nguyen, M.A. Saleh, Results Chem. 2 (2020) 100085.
[45] T. Frenzel, M. Kadic, M. Wegener, Science 358 (2017) 1072–1074.
[46] T. Frenzel et al., Commun. Mater. 2 (2021) 1–9.
[47] T. Frenzel et al., Nat. Commun. 10 (2019) 3384.
[48] J.M. McCracken et al., Adv. Funct. Mater. 31 (2021) 2100564.
[49] T. Frenzel et al., Sci. Rep. 11 (2021) 2304.